

See discussions, stats, and author profiles for this publication at: <https://www.researchgate.net/publication/281667962>

Fusion Zone Microstructure and Geometry in Complete-Joint-Penetration Laser-Arc Hybrid Welding of Low-Alloy Steel

Article in *Welding Journal* · April 2015

CITATION

1

READS

173

4 authors, including:



[Huiliang Wei](#)

Pennsylvania State University

17 PUBLICATIONS 48 CITATIONS

[SEE PROFILE](#)



[Todd A Palmer](#)

Pennsylvania State University

104 PUBLICATIONS 1,138 CITATIONS

[SEE PROFILE](#)



[Tarasankar Debroy](#)

Pennsylvania State University

286 PUBLICATIONS 7,782 CITATIONS

[SEE PROFILE](#)

Some of the authors of this publication are also working on these related projects:



Digital twin of laser assisted additive manufacturing [View project](#)

Fusion Zone Microstructure and Geometry in Complete-Joint-Penetration Laser-Arc Hybrid Welding of Low-Alloy Steel

A process map indicates a martensite-free microstructure can be maintained over a wide range of welding parameters

BY H. L. WEI, J. J. BLECHER, T. A. PALMER, AND T. DEBROY

ABSTRACT

The fusion zone geometry and microstructure in complete-joint-penetration hybrid laser gas metal arc welds of a low-alloy steel are examined experimentally and theoretically. Weld geometry and spatially variable cooling rates are investigated using a three-dimensional heat transfer and fluid flow model. Experimentally measured microstructures are compared with those estimated from a microstructure model based on kinetics and thermodynamics of phase transformations, for a range of laser arc separation distances and heat inputs. Considerable variations in both cooling rates and microstructure were observed for the range of process parameters utilized. In fact, the experimental results and calculations show that for the same heat input, a predominantly ferritic and predominantly martensitic microstructure can be obtained, depending on the laser arc separation distance and resulting cooling rate. A process map is constructed showing the effect of welding speed, laser power, and laser arc separation distance on cooling rates and microconstituent volume fractions. The map indicates a martensite-free microstructure can be maintained over a wide range of welding parameters.

KEYWORDS

- Hybrid Welding • Heat Transfer and Fluid Flow • Microstructure
- Complete Joint Penetration • Laser • Gas Metal Arc • Cooling Rate

Introduction

Hybrid laser-arc welding is a process that combines laser beam welding and conventional arc welding in order to incorporate the benefits of both processes (Refs. 1–4). Hybrid laser-gas metal arc (GMA) welding produces wider weld pools than autogenous laser welding, and deeper weld penetration than GMA welding with the same parameters (Refs. 5–8). The combination of laser and arc energy sources allows for complete-joint-penetration welds to be achieved at significantly higher welding velocities in a single pass, while at the same time allowing large root openings in weld joints to be bridged (Refs. 9, 10). As a result, welding productivity can be

greatly enhanced over that achieved by either laser or GMA welding alone (Refs. 11–13). In addition, hybrid laser-GMA welding has significant advantages in acquiring the desired weld metal microstructures, since lower cooling rates can be more easily obtained than in autogenous laser welding. However, martensite, which has very low ductility and toughness (Ref. 14), can still form in hybrid welding (Ref. 15).

Previous work on the hybrid laser-GMA welding of steels has largely focused on the experimental postcharacterization of weld geometries, microstructures, and mechanical properties (Refs. 15–21). However, these postmortem evaluations provide little detail on the evolution of weld pool geometries and the cooling rates with-

in the fusion zone. In order to understand and predict weld metal microstructural evolution, the thermal cycles experienced during these welding processes must be known. The interactions between the heat sources and materials during complete-joint-penetration hybrid laser-GMA welding lead to rapid thermal cycles in the weld pool, which in turn impacts microstructure evolution. Phase transformations during cooling in the weld fusion zone have been extensively investigated both experimentally and theoretically. Bhadeshia et al. developed a phase transformation model (Refs. 22–24) based on thermodynamics and phase transformation kinetics. This model can quantitatively predict the microstructures and properties of weld deposits for different alloy compositions, cooling rates, and prior austenite grain sizes.

Direct measurement of temperature profiles in the interior of the weld pool still remains a major challenge. On the other hand, a well-tested three-dimensional mathematical model can provide accurate temperature fields and cooling rates at discrete locations throughout the fusion zone (Refs. 25, 26). Several studies focused on the numerical modeling of the fluid flow and heat transfer conditions within the molten weld pool of hybrid laser-arc welding (Refs. 6, 27). Ribic et al. (Ref. 27) numerically studied the effect of laser arc separation distance and laser power on heat transfer and fluid flow in partial-penetration hybrid laser-gas tungsten arc (GTA) welding by using a three-dimensional numerical model. They found that the distance between the laser and arc signifi-

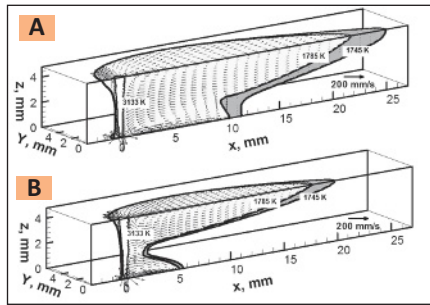


Fig. 1 — Top surface and symmetry plane of weld pool with temperature contours and velocity fields for the following: A — Welding speed of 20.0 mm/s, laser arc separation distance of 1 mm; B — welding speed of 30.0 mm/s, laser arc separation distance of 1 mm.

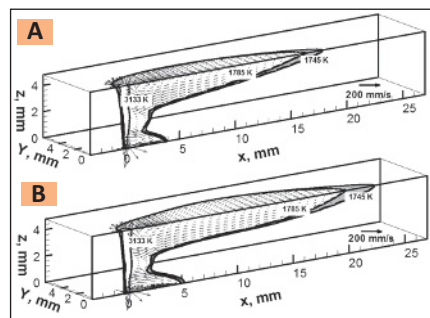


Fig. 3 — Top surface and symmetry plane of weld pool with temperature contours and velocity vectors for the following: A — Welding speed of 40.0 mm/s, laser arc separation distance of 1 mm; B — welding speed of 40.0 mm/s, laser arc separation distance of 5 mm.

cantly affected the cooling rates and that the weld penetration was maximized at an optimal laser arc separation distance (Ref. 27). Cho et al. (Ref. 6) simulated the molten weld pool geometry in laser-arc hybrid welding by solving the equations of continuity, momentum, and energy using a commercial package. They reported that the width of the weld was determined mainly by the GMA heat source and the penetration depth was strongly influenced by the laser (Ref. 6). However, there are very few systematic studies focused on the numerical simulation of

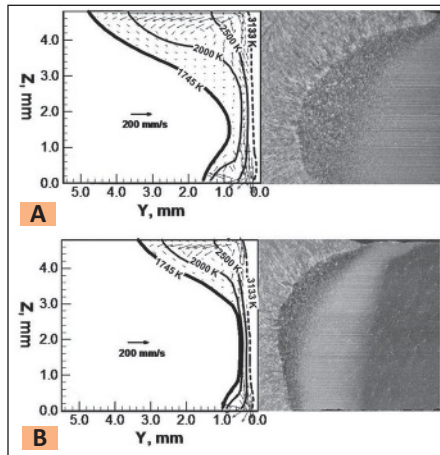


Fig. 2 — Comparison of experimental and simulated weld cross sections for the hybrid laser-GMA complete-joint-penetration welding of DH 36 steel for the following: A — Welding speed of 20.0 mm/s, laser arc separation distance of 1 mm; B — welding speed of 30.0 mm/s, laser arc separation distance of 1 mm.

weld profile evolution, cooling rates within the fusion zone, and the corresponding influence on the weld metal microstructures in complete-joint-penetration hybrid laser-GMA welding. The previous numerical studies (Refs. 6, 27) have discussed partial-penetration hybrid welding, where the fluid flow and heat transfer at the bottom of the molten weld pool are significantly different than those in complete-joint-penetration welding.

In this work, the evolution of macro- and microstructures of complete-joint-penetration laser-GMA hybrid welds in DH 36 steel is analyzed using fundamental transport phenomena and phase transformation theory. A three-dimensional heat transfer and fluid flow model has been developed to study the effect of welding velocity and laser arc separation distance on weld geometries and cooling rates. Using the calculated cooling rates from the heat transfer and fluid flow model, a phase transformation model (Refs. 22–24) based on thermodynamics and phase transformation kinetics is used to provide a

quantitative description of the final microstructures of the weld metal. The computed volume fractions of the weld metal allotriomorphic ferrite, Widmanstätten ferrite, acicular ferrite, and martensite are validated with corresponding experimental results for various welding conditions. The combined models are used to construct process maps capable of predicting the effect of welding parameters on resulting cooling rates and microstructures.

Experimental Procedure

Bead-on-plate complete-joint-penetration hybrid laser-GMA welds were made on 4.8-mm-thick DH 36 steel. An IPG Photonics® YLR-12000-L ytterbium fiber laser with a Precitec® YW50 welding head and a Lincoln Electric® Power Wave 455 M/STT welding power source with a Binzel® WH 455D water-cooled welding gun were used for hybrid welding. The maximum power of the fiber laser is 12 kW, with a wavelength of 1070–1080 nm. The optics system utilizes collimating and focusing lenses with 200- and 500-mm focal lengths, respectively. The laser is transported to the welding head through a 200- μ m-diameter process fiber. The focal spot of the laser beam in the absence of plasma was approximately 0.56 mm in diameter. The laser was focused 8 mm above the surface of the plate. The laser power used in the welding experiments was fixed at 5.0 kW for all the cases. The electrode was 0.045-in.- (1.1-mm-) diameter ER70S-6 wire. The chemical compositions of DH 36 steel and ER70S-6 welding wire are given in Table 1. The metal transfer mode for the welding wire was in spray mode. The shielding gas was a mixture of 95% argon and 5% CO₂ with a flow rate of 95 ft³/h (44.8 L/min). The welding velocities and laser arc separation distances were varied to study their effects on the weld profiles and weld metal microstructures. The key welding parameters are listed in Table 2. The top and bottom surfaces of the plate were

Table 1 — Chemical Composition of Base Metal DH 36 Steel (Ref. 10) and Welding Wire ER 70S-6 (wt-%)

	C	Mn	Si	Ni	Mo	Cr	V	P	S	Al	Nb	Ti	Cu
Base Metal	0.06	1.39	0.19	0.14	0.03	0.11	0.06	0.011	0.004	0.025	0.01	0.01	0.25
Welding Wire	0.09	1.63	0.90	0.05	0.05	0.05	0.05	0.007	0.007	0.000	0.00	0.00	0.20

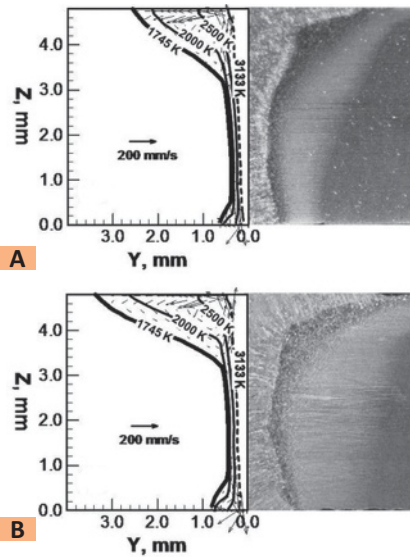


Fig. 4 — Comparison of experimental and simulated weld cross sections for the hybrid laser-GMA complete-joint-penetration welding of DH 36 steel for the following: A — Welding speed of 40.0 mm/s, laser arc separation distance of 1 mm; B — welding speed of 40.0 mm/s, laser arc separation distance of 5 mm.

ground to remove scale prior to welding in order to avoid weld root defects during complete-joint-penetration welding. The sides of the plate were supported, so the welds were made without contacting the table below. Selected welds were sectioned, polished, etched, and photographed to reveal the weld fusion zone profile and microstructures. The volume fractions of selected microconstituents in the weld metal are determined by using the point counting method following the International Institute of Welding (IIW) guidelines (Ref. 28).

Mathematical Model

A three-dimensional heat transfer and fluid flow model for complete-joint-penetration hybrid laser-GMA welding was developed by modifying previous numerical simulation work (Refs. 27, 29, 31). Zhao et al. (Ref. 31) developed a transport phenomena-based numerical model to predict the keyhole geometry and temperature profiles in the weldment during keyhole laser welding. Rai et al. (Ref. 29) developed a convective heat transfer model for both partial and complete-joint-penetration keyhole mode laser welding of a structural steel based on the work of Zhao et al. (Ref.

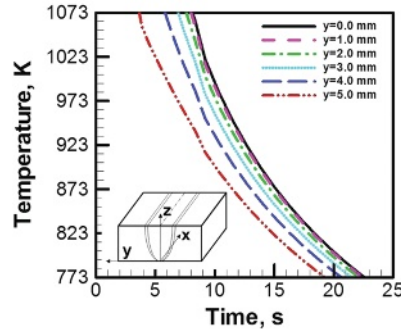


Fig. 5 — Calculated cooling curves at different y locations on the top surface of the fusion zone of weld 1 with welding speed of 20.0 mm/s, laser arc separation distance of 1 mm. The symbol y represents the distance from the weld centerline.

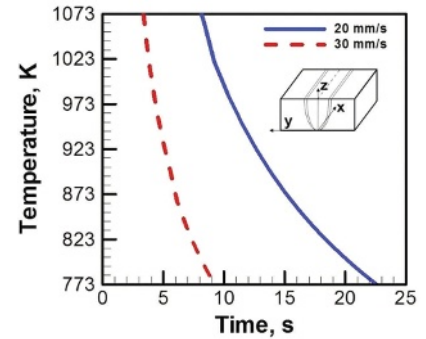


Fig. 6 — Comparison of the calculated cooling rates of the top center fusion zone for weld 1 with welding speed of 20.0 mm/s, laser arc separation distance of 1 mm, and weld 2 with welding speed of 30.0 mm/s, laser arc separation distance of 1 mm.

31). Ribic et al. (Ref. 27) proposed a three-dimensional heat transfer and fluid flow model for partial-penetration hybrid laser-GTA welding. In this work, complete-joint-penetration hybrid laser-GMA welding is studied. Marangoni force-driven velocity boundary conditions at the bottom surface are assumed, which is different from that of partial-penetration hybrid welding. In addition, the heat transfer from the metal droplets during GMAW is integrated into the numerical model for hybrid laser-GMA welding. The material properties used in order to complete the welding calculations are given in Table 3. Details of the numerical simulation model are presented below.

Calculation of Keyhole Profile

The keyhole geometry is calculated using a model that considers material properties, welding process parameters, and specimen geometries. The detailed information about the model is available elsewhere (Refs. 30, 31) and only the salient features are presented here. The keyhole profile is calculated based on a point by point energy balance at the keyhole walls and is determined iteratively. Multiple reflections of the

laser beam within the keyhole are assumed and the number of reflections is dependent on the keyhole geometry. The keyhole wall local temperature is taken as the boiling point of the alloy (Refs. 30, 31). Planar heat conduction from the keyhole wall into the workpiece is assumed due to the significantly higher temperature gradient in all directions in the horizontal plane compared to the vertical directions. Once the profile calculation is completed, the temperature distribution from the keyhole model is stored in a data file with all temperatures inside the keyhole assigned the boiling point temperature. This file is read into the heat transfer and fluid flow model, and at each horizontal x-y plane, the keyhole boundary is identified by a minimum and a maximum x value for any y value.

Heat Transfer in Weld Pool and Boundary Conditions

After the calculation of the keyhole profile, equations of conservation of mass, momentum, and energy are solved in three dimensions in the heat transfer and fluid flow model. Details about this model are available in the literature (Refs. 22, 23, 29) and only the

Table 2 — Welding Process Parameters for Complete-Joint-Penetration Hybrid Laser GMA Welding of DH 36 Steel

Weld Number	Laser Power (kW)	Arc Current (A)	Arc Voltage (V)	Welding Speed (mm/s)	Laser Arc Separation (mm)
1	5.0	248	31	20.0	1.0
2	5.0	235	31	30.0	1.0
3	5.0	232	31	40.0	1.0
4	5.0	232	31	40.0	5.0

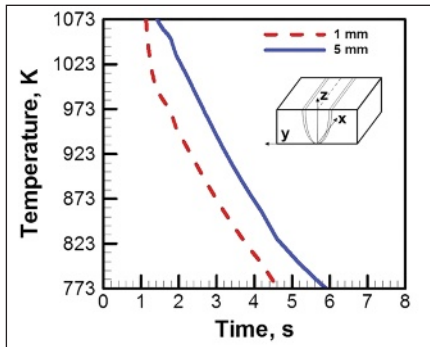


Fig. 7 — Comparison of the calculated cooling rates of the fusion zone located 1 mm above the bottom surface for weld 3 with welding speed of 40.0 mm/s, laser arc separation distance of 1 mm, and weld 4 with welding speed of 40.0 mm/s, laser arc separation distance of 5 mm.

salient features are presented here. The molten metal is assumed to be an incompressible, laminar, and Newtonian fluid. The liquid metal flow in the weld pool can be represented by the following momentum conservation equation (Refs. 30, 31):

$$\rho \frac{\partial u_j}{\partial t} + \rho \frac{\partial(u_i u_j)}{\partial x_i} = \frac{\partial}{\partial x_i} \left(\mu \frac{\partial u_j}{\partial x_i} \right) + S_j \quad (1)$$

where ρ is the density, t is the time, x_i is the distance along the i th ($i = 1, 2,$ and 3) orthogonal direction, u_j is the velocity component along the j direction, μ is the effective viscosity, and S_j is the source term for the j^{th} momentum equation and is given as

$$S_j = -\frac{\partial p}{\partial x_j} + \frac{\partial}{\partial x_j} \left(\mu \frac{\partial u_j}{\partial x_j} \right) - C \left(\frac{(1-f_L)^2}{f_L^3 + B} \right) u_j + \rho g \beta (T - T_{ref}) - \rho U \frac{\partial u_j}{\partial x_j} \quad (2)$$

where p represents pressure, U is the welding speed, and β is the coefficient of volume expansion. The third term represents the frictional dissipation in the mushy zone according to the Carman-Kozeny equation for flow through a porous media (Refs. 32, 33) where f_L is the liquid fraction, B is a very small computational constant to avoid division by zero, and C is a constant accounting for the mushy zone morpholo-

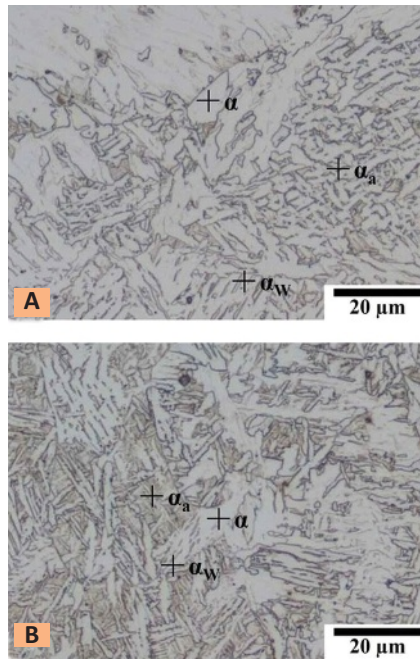


Fig. 8 — Comparison of the optical microstructures of the top center of the fusion zone by different welding speeds. Magnification 500x. A — Welding speed of 20.0 mm/s, laser arc separation distance of 1 mm; B — welding speed of 30.0 mm/s, laser arc separation distance of 1 mm. The symbols α , α_w , and α_a represent allotriomorphic, Widmanstätten, and acicular ferrite, respectively.

gy [a value of 1.6×10^4 was used in the present study (Ref. 34)]. The fourth term is the buoyancy source term (Refs. 23, 34, 35). The last term accounts for the relative motion of the workpiece relative to the laser and arc heat sources (Ref. 23).

The following continuity equation is solved in conjunction with the momentum equation to obtain the pressure field.

$$\frac{\partial(\rho u_i)}{\partial x_i} = 0 \quad (3)$$

In order to trace the weld pool liquid/solid interface, i.e., the phase change, the total enthalpy H is represented by a sum of sensible heat h and latent heat content ΔH , i.e., $H = h + \Delta H$

Table 3 — Material Properties Used for the Calculation of Temperature and Velocity Fields (Ref. 29)

Physical Property	DH 36 Steel
Boiling point (K)	3133
Solidus temperature (K)	1745
Liquidus temperature (K)	1785
Density (kg/m ³)	7200
Thermal conductivity (W/m-K)	21
Inverse Bremsstrahlung absorption coefficient (1/m)	100
Absorption coefficient (flat surface)	0.16
Molecular viscosity (Pa-s)	0.0067
Coefficient of thermal expansion (1/K)	1.96×10^{-5}
Temperature coefficient of surface tension (N/m K)	-0.5×10^{-3}
Enthalpy of solid at melting point (J/kg)	1.20×10^6
Enthalpy of liquid at melting point (J/kg)	1.26×10^6
Specific heat of solid (J/kg K)	710.6
Specific heat of liquid (J/kg K)	836.0

(Ref. 36). The sensible heat h is expressed as $h = \int C_p dT$, where C_p is the specific heat and T is the temperature. The latent heat content ΔH is given as $\Delta H = f_L L$, where L is the latent heat of fusion. The liquid fraction f_L is assumed to vary linearly with temperature for simplicity (Ref. 23) and is given as

$$f_L = \begin{cases} 1 & T > T_L \\ \frac{T - T_S}{T_L - T_S} & T_S \leq T \leq T_L \\ 0 & T < T_S \end{cases} \quad (4)$$

where T_L and T_S are the liquidus and solidus temperature, respectively. Thus, the thermal energy transportation in the weld workpiece can be expressed by the following modified energy equation:

$$\rho \frac{\partial h}{\partial t} + \rho \frac{\partial(u_i, h)}{\partial x_i} = \frac{\partial}{\partial x_i} \left(\frac{k}{C_p} \frac{\partial h}{\partial x_i} \right) + S_h \quad (5)$$

where k is the thermal conductivity. The source term S_h is due to the latent heat content and is given as

$$S_h = -\rho \frac{\partial(\Delta H)}{\partial t} - \rho \frac{\partial(u_i \Delta H)}{\partial x_i} - \rho U \frac{\partial h}{\partial x_i} - \rho U \frac{\partial \Delta H}{\partial x_i} \quad (6)$$

The heat transfer and fluid flow equations were solved for the complete workpiece. For the region inside the keyhole, the coefficients and source terms in the equations were adjusted to obtain boiling point temperature and zero fluid velocities.

A 3D Cartesian coordinate system is used in the calculation. Only half of the workpiece is considered since the weld is symmetrical about the weld centerline. At the bottom of the weld pool, Marangoni force-driven fluid velocity boundary conditions are assumed for complete-joint-penetration welding. A $187 \times 77 \times 26$ grid system is used in the calculation and the corresponding calculation domain dimensions are 522 mm in length, 36 mm in half-width, and 4.8 mm in depth. The interactions between laser and arc as well as the heat transfer and fluid flow within the weld pool are affected by the separation distance between laser and arc. In the numerical model, the effect of arc energy on the formation of the keyhole and the ener-

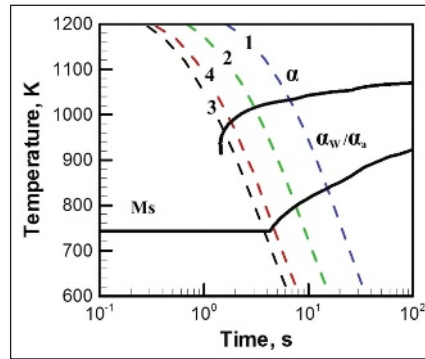


Fig. 10 — Calculated CCT diagrams with the cooling curves superimposed. Cooling rates are taken at the top center of welds with 1 mm laser arc separation distance and 20 and 30 mm/s welding speed (welds 1 and 2, respectively). Cooling rates are taken at 1 mm from the bottom surface of welds with 40 mm/s welding speed and 1 and 5 mm laser arc separation (welds 3 and 4, respectively). The symbols α , α_w and α_a represent allotriomorphic, Widmanstätten, and acicular ferrite, respectively. M_s is the starting temperature for martensite formation.

gy transportation from the keyhole wall to the liquid weld pool are calculated. However, the laser-arc interaction, which has been characterized experimentally with optical emission spectroscopy (Ref. 37), is not rigorously simulated here.

During laser-GMA hybrid welding, the rates of heat, mass, and momentum transport are often enhanced because of the presence of fluctuating velocities in the weld pool. The contribution of the fluctuating velocities is considered by the incorporation of a turbulence model that provides a systematic framework for calculating effective viscosity and thermal conductivity (Refs. 32, 33). The values of these properties vary with the location in the weld pool and depend on the local fluid flow characteristics. In this work, a turbulence model based on Prandtl's mixing length hypothesis (Ref. 32) is used to estimate the turbulent viscosity.

Calculation of Heat Transfer from GMA Metal Droplets

The hot molten metal droplets produced by the GMAW process impinge into the weld pool at high velocities and carry a significant amount of heat into the liquid weld pool (Refs. 34–36, 38, 39). The heat transfer from the metal

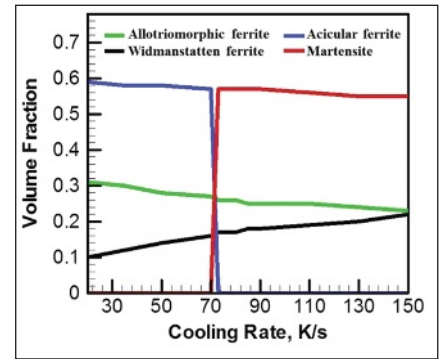


Fig. 11 — Variation of the volume fractions of allotriomorphic ferrite, Widmanstätten ferrite, acicular ferrite, and martensite with different cooling rates.

droplets was simulated by considering a cylindrical heat source with a time-averaged uniform power density (S_v). The use of a cylindrical volumetric heat source assumes the spray transfer mode of the droplets, which is consistent with the welding conditions in the present study.

In order to calculate S_v , the radius of the heat source, its effective height, and the total sensible heat input by the droplets are required. The radius of the volumetric heat source is assumed to be twice that of the droplet radius, and the effective height, d , is calculated from the following equation (Refs. 34, 38, 39):

$$d = h_v - x_v + D_d \quad (7)$$

where h_v is the estimated height of the cavity caused by the impact of metal droplets, x_v is the distance traveled by the center of the two successive impinging droplets, and D_d is the droplet diameter. The total sensible heat input from the metal droplets, Q_d , is given as (Ref. 34)

$$Q_d = \pi \rho_w r_w^2 w_f C_p (T_d - T_l) \quad (8)$$

where ρ_w is the density of the electrode wire, r_w is the radius of the wire, w_f is the wire feeding rate, T_d is the droplet temperature, and T_l is the liquid temperature.

The values of h_v and x_v in Equation 7 are calculated based on an energy balance as (Ref. 39):

$$h_v = -\frac{2\gamma}{D_d \rho g} + \sqrt{\left(\frac{2\gamma}{D_d \rho g} \right)^2 + \frac{D_d v_d^2}{6g}} \quad (9)$$

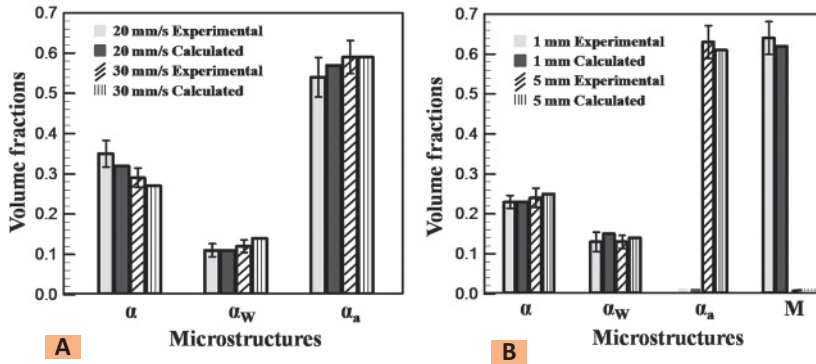


Fig. 12 — Comparison of the experimental and calculated microstructure volume fractions of the weld metal for weld 1 with welding speed of 20.0 mm/s, laser arc separation distance of 1 mm; weld 2 with welding speed of 30.0 mm/s, laser arc separation distance of 1 mm; weld 3 with welding speed of 40.0 mm/s, laser arc separation distance of 1 mm; and weld 4 with welding speed of 40.0 mm/s, laser arc separation distance of 5 mm. The symbols α , α_w and α_a represent allotriomorphic, Widmanstätten, and acicular ferrite, respectively.

$$x_v = \left(h_v + \frac{2\gamma}{D_d \rho g} \right) \left\{ 1 - \cos \left[\left(\frac{g}{h_v} \right)^{1/2} \Delta t \right] \right\} \quad (10)$$

where γ is the surface tension of the molten metal, ρ is the density, g is acceleration due to gravity, v_d is the droplet impingement velocity, and Δt is the time interval between two successive drops, which is the inverse of the droplet transfer frequency. As shown in Equations 9 and 10, calculation of the dimensions of the volumetric heat source requires the knowledge of the droplet transfer frequency, radius, and impingement velocity, which can be determined from literature (Refs. 34, 38, 39). From the calculated values of Q_d , D_d , and d , the time-averaged power density of the volumetric heat source, S_v , is calculated as follows (Ref. 34)

$$S_v = \frac{Q_d}{\pi D_d^2 d} \quad (11)$$

Equation 11 is only valid for grid points within the cylindrical heat source, and the power density is zero outside the cylinder. Free surface calculation of the weld top and bottom surface is not considered in the current model, and the simplification of flat pool surfaces is not expected to affect the calculated weld shape and microstructure significantly (Ref. 40).

Phase Transformation Calculation

In the weld fusion zone of low-alloy steels, allotriomorphic ferrite is the first phase to form and it nucleates heterogeneously at the boundaries of the columnar austenite grains during cooling. It is a reconstructive transformation involving diffusion (Ref. 26). As temperature decreases, diffusion becomes sluggish and gives way to a displacive transformation. At relatively low undercoolings, plates of Widmanstätten ferrite form by a displacive mechanism. At further undercoolings, bainite nucleates and grows in the form of sheaves of small platelets. Acicular ferrite nucleates intragranularly around inclusions inside the austenite (Ref. 26). The diffusionless martensite transformation may take place if the cooling rate is high enough.

The isothermal time-temperature-transformation (TTT) and continuous-cooling-transformation (CCT) diagrams together with various transformation starting temperatures are calculated using the phase transformation model based on thermodynamics and phase transformation kinetics with weld deposit compositions as input variables (Refs. 22–24). The incubation times for both reconstructive and displacive transformations are calculated by Russell’s expression:

$$\tau = T^a \times (\Delta G_{max})^b \times \exp\left(\frac{c}{T}\right) \times d \quad (12)$$

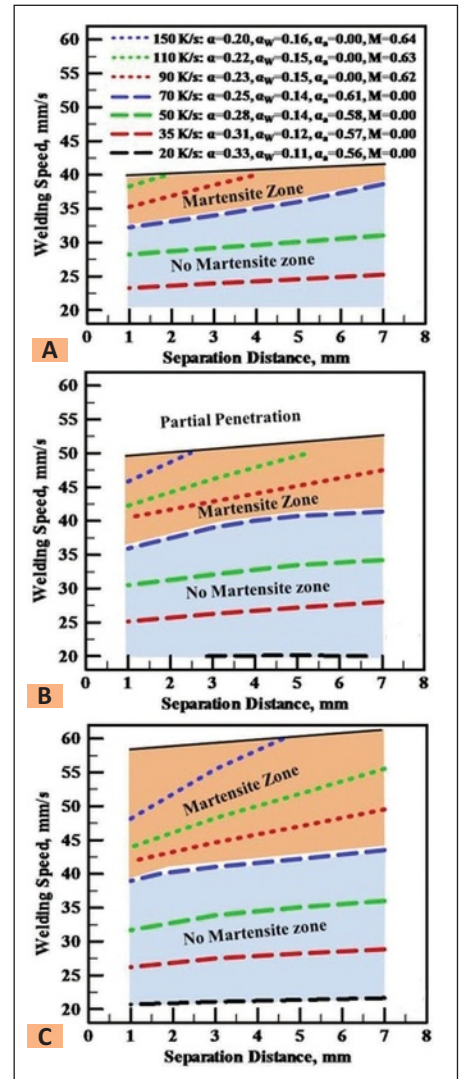


Fig. 13 — Computed volume fractions of allotriomorphic, Widmanstätten, and acicular ferrite, and martensite with corresponding cooling rates from 1073 to 773 K of the fusion zone lower center as a function of laser arc separation distance and welding speed by different laser powers. A — Laser power = 4.0 kW, arc current = 232 A, arc voltage = 31 V; B — laser power = 5.0 kW, arc current = 232 A, arc voltage = 31 V; C — laser power = 6.0 kW, arc current = 232 A, arc voltage = 31 V. The symbols α , α_w , α_a , and M represent allotriomorphic, Widmanstätten, and acicular ferrite, and martensite, respectively.

where τ is the incubation time for a transformation, T is the temperature, ΔG_{max} is the maximum driving force for nucleation, and a , b , c , and d are constants. The details of calculation of ΔG_{max} and determination of a , b , c , and d are given in the literature (Ref. 22).

The CCT diagrams are calculated from the corresponding TTT diagrams

based on the Scheil additive rule (Ref. 41):

$$\int_0^t \frac{dt}{t_a(T)} = 1 \quad (13)$$

where t_a is the incubation time required to reach a specified state on a TTT diagram for isothermal reactions, t is the time to that stage for the nonisothermal reactions, and dt is the time interval at temperature T . In this procedure, the total time to reach a specified state of transformation for nonisothermal reactions is obtained by adding the fractions of time to reach this stage isothermally until the sum reaches unity.

The inclusion of the weld deposit compositions also leads to the calculation of the appropriate part of the phase diagram needed to obtain para-equilibrium compositions for kinetic analysis. These data are combined with austenite grain parameters and the computed cooling curves from the heat transfer and fluid flow model to calculate the volume fractions of allotriomorphic, Widmanstätten ferrite, acicular ferrite, and martensite (Ref. 23). The modeling results are used to better understand the experimentally observed microstructures of the weld metal in complete-joint-penetration hybrid laser-GMA welding.

Results and Discussion

Calculated Temperature and Velocity Fields

The effects of welding speed and laser arc separation distance on weld profiles and temperature and velocity fields are studied separately for complete-joint-penetration hybrid laser-GMA welding. Both these parameters have been shown to significantly affect the weld quality and welding productivity. Figure 1 shows the calculated temperature and fluid flow fields in three dimensions when the welding speed increases from 20 to 30 mm/s with a constant laser arc separation distance of 1 mm. The temperature is indicated by contour lines and the velocity field is represented by arrows. There is an intense temperature gradient on the top and bottom surfaces of the weld pool because the temperature of the liquid metal at the keyhole wall equals the boiling point, while the liquid metal at

the weld pool boundary remains at the solidus temperature. The molten metal moves radially outward for both the top and bottom surfaces because of the Marangoni convection produced by the spatial gradient of surface tension resulting from the temperature gradient. The maximum outward flow velocities of the top surface are 155.6 and 194.2 mm/s for welding speeds of 20 and 30 mm/s, respectively. The momentum is then transferred by viscous dissipation to the inner layers of the weld pool adjacent to the surface.

The comparison between these calculated and experimental weld pool geometries is shown in Fig. 2. The top surface width decreases from 9.6 to 7.0 mm, and the bottom surface width decreases from 3.6 to 2.0 mm when the welding speed increases from 20 to 30 mm/s. The boiling point contours indicate the cross-sectional geometry of the keyhole, while the solidus temperature contours indicate the fusion zone boundary. It is observed that the widths of the top and bottom surfaces, as well as the shape of the fusion zone predicted by the heat transfer and fluid flow model, agreed well with the corresponding experimental results. The weld pool dimensions decrease significantly with the increasing welding speed as the top surface widens due to Marangoni convection. Furthermore, the bottom width is also larger than the minimum weld profile width at the middle of the plate thickness, indicating the significant effect of convective heat transfer.

Figure 3 shows the calculated temperature and fluid flow fields when the laser arc separation distance increases from 1 to 5 mm with a welding speed of 40 mm/s. When the laser arc separation distance is changed, the nominal total heat input of the welding process is constant, while the heat input decreases from 0.63 to 0.41 kJ/mm with a welding velocity increase from 20 to 30 mm/s, as shown in Fig. 2. The computed length of the weld pool increases from 18 to 23 mm with the increasing laser arc separation distance. The heat from the laser and arc as well as the droplet is more concentrated near the laser beam incident point at shorter laser arc separation distance. The heat distribution over the top surface of the weld pool significantly changes when the arc axis is further separated from the laser beam. The top part of the liq-

uid weld pool is stretched and the distance along the welding direction from the maximum weld width to the laser beam incidental point is significantly increased.

Figure 4 shows the comparison between these calculated and experimental weld pool geometries. The top surface width increases from 5.1 to 6.8 mm, and the bottom surface width increases from 1.2 to 1.6 mm when the laser arc separation distance increases from 1 to 5 mm. It can be observed from Figs. 1 and 3 that the effects of welding speed and laser arc separation distance on the weld profiles are different. When the welding speed increases from 20 to 30 mm/s, the weld pool shrinks significantly in all locations along the weld depth. However, only the top part of the weld pool significantly increases when the laser arc separation distance increases from 1 to 5 mm. The bottom part has a slight change and the middle part of the weld pool is almost unaffected by the laser arc separation distance. Changes in these processing conditions impact the resulting weld pool geometries in different ways. For example, the increase of the welding speed reduces the net energy absorbed by the workpiece. On the other hand, the increase of the laser arc separation distance mainly influences the energy distribution of the heat sources.

Cooling Rates

The cooling rates over the austenite decomposition range from 1073 to 773 K within the weld fusion zone are calculated using this same heat transfer and fluid flow model. The calculated cooling rates are then used in the modeling of the weld metal microstructures of low-alloy steels. Figure 5 shows the calculated cooling curves between 773 and 1073 K at different locations on the top surface of the weld with a welding speed of 20 mm/s. It can be seen that the cooling rates are almost independent of position. The cooling rates within the fusion zone and the cooling rate in the heat-affected zone (HAZ) are both at a level of approximately 20 K/s. These similarities in cooling rates allow a single cooling condition to be assumed for each horizontal plane across the weld depth.

The comparison of the calculated

cooling curves at the top surface of the fusion zone for welding velocities of 20 and 30 mm/s and a 1-mm separation distance are shown in Fig. 6. The calculated cooling rate between 1073 and 773 K increases from 21.3 to 48.4 K/s with the increasing weld speed. The corresponding cooling times are 14.1 and 6.2 s, respectively. As expected, the cooling rate increases with increasing welding speed and resulting decrease in heat input.

The calculated cooling curves between 1073 and 773 K along the centerline 1.0 mm above the bottom surface of the weld for laser arc separation distances of 1 and 5 mm at a welding speed of 40 mm/s are shown in Fig. 7. This position is chosen because the width of the weld pool is the smallest at this depth, which indicates that the weld metal at this region is more prone to contain martensite. The calculated cooling rates from 1073 to 773 K are 83.3 and 66.7 K/s when the laser arc separation distance increases from 1 to 5 mm. The corresponding cooling times are 3.6 and 4.5 s, respectively. Ribic et al. (Ref. 27) reported that for hybrid laser-GTA welding with heat input of 0.10 kJ/mm, the cooling time from 1073 to 773 K increased from 0.45 to 0.75 s with the increase of laser arc separation distance from 3.5 to 9.2 mm. As can be seen from Fig. 3A, B, the weld pool length increases with the increasing laser arc separation distance. The isothermals also expand for regions beyond the liquid weld pool so that the spatial gradient of temperature decreases for the temperature range from 1073 to 773 K. Therefore, the cooling rate decreases with increasing laser arc separation distance, which is consistent with the result reported by Ribic et al. (Ref. 27).

In order to validate the calculation of the cooling rates between 1073 and 773 K, the calculated cooling rates for different welding conditions are compared with the results available in the literature that examine the effects of changes in heat input and plate thickness on the cooling rate during arc welding (Ref. 42). The literature results show the cooling time from 1073 to 773 K for the welding speeds of 20, 30, and 40 mm/s are approximately 13.1, 6.0, and 3.9 s, compared with the values of 14.1, 6.2, and 3.6 s calculated by the heat transfer and fluid flow model. Therefore, the cooling rates between 1073

and 773 K obtained from the literature and the 3D heat transfer and fluid flow model show good agreement.

Microstructures

The comparison of the fusion zone microstructures located at the top surface of the weld for welding speeds of 20 and 30 mm/s at laser arc separation distance of 1 mm is shown in Fig. 8. For a welding speed of 20 mm/s, the microstructure contains 35% allotriomorphic ferrite, 11% Widmanstätten ferrite, and 54% acicular ferrite. When the welding speed increases to 30 mm/s, the amount of allotriomorphic ferrite decreases to 29%, Widmanstätten ferrite increases to 12%, and acicular ferrite increases to 59%. The average length of the acicular ferrite decreases from 13.1 to 7.1 μm and the width decreases from 3.1 to 1.2 μm when the welding speed increases from 20 to 30 mm/s. The hardness testing results show the microhardness value increases from 223 to 248 HV. The average microhardness of the base metal is 174 ± 11 HV. The differences in microstructure contribute to the higher microhardness of the weld metal with a higher welding speed.

The comparison of the fusion zone microstructures located 1.0 mm above the bottom surface of the weld for a laser arc separation distance of 1 and 5 mm at a welding speed of 40 mm/s is shown in Fig. 9. The volume fraction of martensite is about 64% for the laser arc separation distance of 1 mm, compared with a separation distance of 5 mm when no martensite is present. The amounts of allotriomorphic ferrite and Widmanstätten ferrite are about 23 and 13%, respectively, for 1-mm separation distance. The volume fraction of acicular ferrite is about 63%, and the amounts of allotriomorphic ferrite and Widmanstätten ferrite are about 24 and 13%, respectively, for a laser arc separation distance of 5 mm. The microhardness decreases from 283 to 238 HV when the laser arc separation distance increases from 1 to 5 mm. The higher microhardness indicates martensite is present and signifies a lower toughness of the weld (Refs. 21, 43, 44), which is detrimental to the mechanical properties of the joint.

Figure 10 shows the CCT diagrams computed from the TTT diagram based

on the Scheil additive rule, superimposed with the cooling curves at selected locations in the four welds. The cooling curves of the welds with welding speeds of 20 and 30 mm/s at a laser arc separation distance of 1 mm both intercept with the diffusive and displacive transformation curves, so allotriomorphic ferrite, Widmanstätten ferrite, bainite, and acicular ferrite are expected. The cooling curve of the weld with a laser arc separation distance of 1 mm at the welding speed of 40 mm/s intercepts with the upper C curve and the martensite transformation line while the cooling curve for the weld with a laser arc separation distance of 5 mm at the welding speed of 40 mm/s intercepts with both the upper and lower C curves but not the martensite transformation line. As a result, martensite is expected with the laser arc separation distance of 1 mm but not for the laser arc separation distance of 5 mm, although the net heat input of the welding process is identical.

The variation of the calculated volume fractions of allotriomorphic and Widmanstätten ferrite, acicular ferrite, and martensite with cooling rates is shown in Fig. 11. For the composition of DH 36 steel and austenite grain sizes observed in the experimental welds, acicular ferrite is the predominant phase, comprising nearly 60% of the microstructure up to the critical cooling rate for martensite. Widmanstätten ferrite increases with cooling rate at the expense of allotriomorphic ferrite. These two phases combine to make up 40% of the microstructure. The calculated results are consistent with the data reported in previous work (Ref. 24).

Both the experimentally measured and calculated quantitative volume fractions of different phases of the four welds are shown in Fig. 12. Good agreement between the two sets of data is observed. Figure 12A shows the volume fractions of allotriomorphic ferrite and acicular ferrite slightly decrease while Widmanstätten ferrite increases with the increasing welding speed. Figure 12B shows the martensite volume fraction is about 52% when the laser arc separation distance is 1 mm, but no martensite is observed when the laser arc separation distance increases to 5 mm. A very small amount of acicular ferrite is observed experimentally for a laser arc

separation distance of 1 mm, compared to 5-mm separation distance when acicular ferrite is the predominant phase.

It should be noted the welding conditions including the heat input are all identical when the laser arc separation distance changes from 1 to 5 mm. The reason for the large difference of the weld metal microstructures with the changing laser arc separation distance lies in the fact that the cooling condition, especially the cooling rate between 1073 and 773 K, significantly decreases when the laser arc separation distance increases from 1 to 5 mm. The cooling rate exceeds the critical cooling rate for martensite transformation with laser arc separation distance of 1 mm while it decreases to a value lower than the critical cooling rate for martensite transformation when the laser arc separation distance increases to 5 mm.

Process Map

In order to further understand the influence of welding parameters on the cooling rates and corresponding volume fractions of the microstructures of the weld fusion zone, a comprehensive process map is presented in Fig. 13. The map considers various combinations of welding speed, laser arc separation distance, and laser power. The arc current and arc voltage are 232 A and 31 V, respectively, for all the welding conditions. The laser powers for Fig. 13A–C are 4, 5, and 6 kW, respectively. The maps show the combinations of separation distance and welding speed that produce a given cooling rate and corresponding microstructure in terms of volume fractions of different phases and microconstituents. The critical cooling rate for martensite transformation is about 71 K/s, which is calculated by the model for microstructure evolution (Refs. 22–24). Cooling rates below 71 K/s are shown in dashed lines as a zone without martensite, while cooling rates greater than 71 K/s are shown in dotted lines as another zone with martensite in Fig. 13. The upper bound on the process maps is the partial penetration line, above which complete penetration is not possible.

In general, welding speed has a greater effect on cooling rate than separation distance, and at low welding speeds of 20 mm/s, the cooling rate is

almost independent of separation distance. The effect of power can also be observed in Fig. 13. As power increases, the cooling rates shift to higher welding speeds for a given separation distance. For example, at 1 mm separation distance, the required welding speeds to obtain a 70 K/s cooling rate are 32 and 39 mm/s for 4 kW and 6 kW laser powers, respectively. It is important to know how cooling rates affect the microstructure. As the cooling rate increases from 20 to 150 K/s, the volume fraction of Widmanstätten ferrite increases from 0.10 to 0.22 at the expense of the allotriomorphic ferrite, which decreases from 0.31 to 0.23. The amount of acicular ferrite decreases from 0.59 to 0.57 from low cooling rates up to the critical cooling rate when acicular ferrite disappears and martensite forms instead.

These maps provide a means for understanding microstructure evolution during hybrid laser-arc welding and can be used to select welding parameters that optimize the weld microstructure or minimize welding time yet limit the formation of martensite. For example, as stated previously, if the power is increased from 4 to 6 kW for a constant separation distance of 1 mm, then the welding speed can be increased by 22% from 32 to 39 mm/s without the formation of martensite. Increasing the separation distance from 1 to 7 mm further increases the possible welding speed to 42 mm/s. Compared to the initial conditions in this example, the total increase in welding speed is 31% due to a 33% increase in laser power and a 6-mm increase in separation distance. The welding speed and the resulting time to make a weld are important. When comparing the costs of hybrid laser-GMA welding with conventional arc welding for pipe joining applications, Reutzel et al. (Ref. 45) found that weld time comprised between 24 and 41% of the total fabrication time, depending on pipe diameter, with other tasks, such as fitup, preparation of the weld, and movement of the part, making up the rest of the time. Additionally, since the welding is occurring with the same cooling rate, there would be no change in the microstructure. The utility of the process map indicates significant promise for understanding the evolution of microstructures in the fusion zone of hybrid laser-GMA complete-joint-penetra-

tion welding by a combination of phase transformation model and the thermal cycles calculated from the heat transfer and fluid flow model.

Summary and Conclusions

The effect of laser arc separation distance and welding speed on fusion zone geometry and microstructure during complete-joint-penetration hybrid laser-gas metal arc welding of low-alloy steel was investigated experimentally and theoretically. A heat transfer and fluid flow model was used to calculate the weld pool geometry and cooling rates, which were applied to a microstructure model to compute the phase fractions of selected microconstituents. Experimental weld geometries and microstructures were compared to the calculated values, and the two sets of data agreed well. The following conclusions can be drawn from this work:

1. The effect of welding speed and laser arc separation distance on weld pool geometry was investigated in complete-joint-penetration hybrid laser-arc welding. The weld length and width both at the top and bottom of the pool increased with increasing laser arc separation distance for the same heat input. The weld pool dimensions decreased with increasing welding speed as expected.
2. Cooling rate was also affected by the hybrid welding parameters. When the welding speed increased, which changed the net heat input, the cooling rate increased. When the laser arc separation distance decreased, which altered the heat distribution of the combined power sources but not the heat input, the cooling rate increased. At high welding speeds, the decrease in separation distance can have a significant enough effect on the cooling rate to form martensite in the microstructure.
3. The experimental weld microstructures consisted of acicular ferrite, allotriomorphic ferrite, Widmanstätten ferrite, and martensite. Martensite existed only in the weld with the laser arc separation distance of 1 mm and a welding speed of 40 mm/s. Acicular ferrite formed at the expense of martensite when the separation distance increased to 5 mm. Increasing the welding speed from 20 to 30 mm/s resulted in a decrease of allotriomorphic

ferrite and an increase in Widmanstätten and acicular ferrite.

4. Utilizing the combined models, a process map has been constructed that illustrates the effects of welding speed, separation distance, and laser power on cooling rate and microconstituent volume fractions. Identical cooling rates and microconstituent volume fractions can be obtained with various combinations of process parameters. In general, welding speed and laser power have a more significant effect on cooling rates than separation distance; however, at high welding speeds, the separation distance can be the deciding factor for martensite formation.

Acknowledgments

The authors would like to thank Mr. Jay Tressler for performing the hybrid welding experiments, Mr. Ed Good and Dr. Jay Keist for assisting with the metallography, and Prof. Lars-Erik Svensson for assisting with the microstructure identification and quantification. This research was performed using funding received from the DOE Office of Nuclear Energy's Nuclear Energy University Programs under Grant Number 120327.

References

1. Steen, W. M. 1980. Arc augmented laser processing of materials. *Journal of Applied Physics* 51(11): 5636–5640.
2. Tusek, J., and Suban, M. 1999. Hybrid welding with arc and laser beam. *Science and Technology of Welding and Joining* 4(5): 308–311.
3. Page, C. J., Devermann, T., Biffin, J., and Blundell, N. 2002. Plasma augmented laser welding and its applications. *Science and Technology of Welding and Joining* 7(1): 1–10.
4. Chen, Y. B., Lei, Z. L., Li, L. Q., and Wu, L. 2006. Experimental study on welding characteristics of CO₂ laser TIG hybrid welding process. *Science and Technology of Welding and Joining* 11(4): 403–411.
5. Zhou, J., and Tsai, H. L. 2008. Modeling of transport phenomena in hybrid laser-MIG keyhole welding. *International Journal of Heat and Mass Transfer* 51(17-18): 4353–4366.
6. Cho, J. H., and Na, S. J. 2009. Three-dimensional analysis of molten pool in GMA-laser hybrid welding. *Welding Journal* 88(2): 35-s to 43-s.
7. Vollertsen, E., Grunenwald, S., Rethmeier, M., Gumenyuk, A., Reisgen, U., and Olschook, S. 2010. Welding thick steel plates with fibre lasers and GMAW. *Welding in the World* 54(3–4): R62–R70.
8. Le Guen, E., Fabbro, R., Carin, M., Coste, F., and Le Masson, P. 2011. Analysis of hybrid Nd:YAG laser-MAG arc welding processes. *Optics and Laser Technology* 43(7): 1155–1166.
9. Cao, X., Wanjara, P., Huang, J., Munro, C., and Nolting, A. 2011. Hybrid fiber laser-arc welding of thick section high strength low alloy steel. *Materials and Design* 32(6): 3399–3413.
10. Roepke, C., Liu, S., Kelly, S., and Martukanitz, R. 2010. Hybrid laser arc welding process evaluation on DH36 and EH36 steel. *Welding Journal* 89(7): 140-s to 150-s.
11. Bagger, C., and Olsen, F. O. 2005. Review of laser hybrid welding. *Journal of Laser Applications* 17(1): 2–14.
12. Gao, M., Zeng, X. Y., and Hu, Q. W. 2006. Effects of welding parameter on melting energy of CO₂ laser-GMA hybrid welding. *Science and Technology of Welding and Joining* 11(5): 517–522.
13. Rao, Z. H., Liao, S. M., and Tsai, H. L. 2011. Modeling of hybrid laser-GMA welding: Review and challenges. *Science and Technology of Welding and Joining* 16(4): 300–305.
14. Callister, W. D., and Rethwisch, D. G. 2009. *Materials Science and Engineering*. Wiley, U.S.A.
15. Roepke, C., and Liu, S. 2009. Hybrid laser arc welding of HY-80 steel. *Welding Journal* 88(8): 159-s to 167-s.
16. Gao, M., Zeng, X. Y., Hu, Q. W., and Yan, J. 2008. Weld microstructure and shape of laser-arc hybrid welding. *Science and Technology of Welding and Joining* 13(2): 106–113.
17. Moore, P. L., Howse, D. S., and Wallach, E. R. 2004. Microstructures and properties of laser-arc hybrid welds and autogenous laser welds in pipeline steels. *Science and Technology of Welding and Joining* 9(4): 314–322.
18. Swanson, P. T., Page, C. J., Read, E., and Wu, H. Z. 2007. Plasma augmented laser welding of 6 mm steel plate. *Science and Technology of Welding and Joining* 12(2): 153–160.
19. Chen, Y. B., Feng, J. C., Li, L. Q., Chang, S., and Ma, G. L. 2013. Microstructure and mechanical properties of a thick-section high-strength steel welded joint by novel double-sided hybrid fibre laser-arc welding. *Materials Science and Engineering A – Structural Materials Properties Microstructure and Processing* 582: 284–293.
20. Gao, M., Zeng, X. Y., Yan, J., and Hu, Q. W. 2008. Microstructure characteristics of laser-MIG hybrid welded mild steel. *Applied Surface Science* 254(18): 5715–5721.
21. McPherson, N. A., Suarez-Fernandez, N., Moon, D. W., Tan, C. P. H., Lee, C. K., and Baker, T. N. 2005. Laser and laser-assisted arc welding process for DH 36 microalloyed steel ship plate. *Science and Technology of Welding and Joining* 10(4): 460–467.
22. Bhadeshia, H. K. D. H. 1982. Thermodynamic analysis of isothermal transformation diagrams. *Metal Science* 16(3): 159–165.
23. Bhadeshia, H. K. D. H., Svensson, L. E., and Grotto, F. 1985. A model for the development of microstructure in low-alloy steel (Fe-Mn-Si-C) weld deposits. *Acta Metallurgica* 33(7): 1271–1283.
24. Bhadeshia, H. K. D. H., and Svensson, L. E. 1993. Modeling the evolution of microstructure in steel weld metal. *Mathematical Modeling of Weld Phenomena*. H. Cerjak and K. E. Eastering, eds. Institute of Materials, London, pp. 109–180.
25. Munda, K., and DebRoy, T. 1996. Numerical prediction of fluid flow and heat transfer in welding with a moving heat source. *Numerical heat transfer, Part A* 29: 115–129.
26. Munda, K., and DebRoy, T. 1993. Calculation of weld metal composition change in high-power conduction mode carbon-dioxide laser welded stainless steels. *Metallurgical Transactions B – Process Metallurgy* 24(1): 145–155.
27. Ribic, B., Rai, R., and DebRoy, T. 2008. Numerical simulation of heat transfer and fluid flow in GTA/Laser hybrid welding. *Science and Technology of Welding and Joining* 13(8): 683–693.
28. International Institute of Welding (IIW), Guide to the light microscope examination of ferritic steel weld metals. 1991. *Welding in the World* 29: 160–176.
29. Rai, R., Kelly, S. M., Martukanitz, R. P., and DebRoy, T. 2008. A convective heat transfer model for partial and full penetration keyhole mode laser welding of a structural steel. *Metallurgical and Materials Transactions A* 39A: 98–112.
30. Kaplan, A. 1994. A model of deep penetration laser welding based on calculation of the keyhole profile. *Journal of Physics D: Applied Physics* 27: 1805–1814.
31. Zhao, H., and DebRoy, T. 2003. Macro-erosivity free aluminum alloy weldments through numerical simulation of keyhole mode laser welding. *Journal of Applied Physics* 93: 10089–10097.
32. Wilcox, D. C. 1993. *Turbulence Modeling for CFD* (California: DCW Industries).
33. Launder, B. E., and Spalding, D. B. 1972. *Lectures in Mathematical Models of Turbulence*. London, UK: Academic Press.
34. Zhang, W., Kim, C. H., and DebRoy, T. 2004. Heat and fluid flow in complex joints during gas metal arc welding — Part II: Application to fillet welding of mild steel. *Journal of Applied Physics* 95(9): 5220–5229.
35. Essers, W. G., and Walter, R. 1981. Heat transfer and penetration mechanisms with GMA and plasma-GMA welding. *Welding Journal* 60(2): 37-s to 42-s.
36. Lancaster, J. F. 1984. *The Physics of Welding*. New York, N.Y.: Pergamon Press.
37. Ribic, B., Burgardt, P., and DebRoy, T. 2011. Optical emission spectroscopy of metal vapor dominated laser-arc hybrid welding plasma. *Journal of Applied Physics* 109(8): 083301.
38. Kumar, S., and Bhaduri, S. C. 1994. Three-dimensional finite element modeling of gas metal arc welding. *Metallurgical and Materials Transactions B* 25B: 435–441.
39. Yang, Z., and DebRoy, T. 1999. Modeling macro- and microstructures of gas-metal-arc welded HSLA-100 steel. *Metallurgical and Materials Transactions B – Process Metallurgy and Materials Processing Science* 30(3): 483–493.
40. Kou, S. 2012. Fluid flow and solidification in welding: Three decades of fundamental research at the university of Wisconsin. *Welding Journal* 91(11): 287-s to 302-s.
41. Takahashi, M., and Bhadeshia, H. K. D. H. 1991. A model for the microstructure of some advanced bainitic steels. *Materials Transactions* 32(8): 689–696.
42. Masubuchi, K. 1980. *Analysis of Welded Structures*. New York, N.Y.: Pergamon Press.
43. Ribic, B., Palmer, T. A., and DebRoy, T. 2009. Problems and issues in laser-arc hybrid welding. *International Materials Reviews* 54(4): 223–244.
44. Sevim, I. 2006. Effect of hardness to fracture toughness for spot welded steel sheets. *Materials and Design* 27(1): 21–30.
45. Reutzel, E. W., Sullivan, M. J., and Mikesic, D. A. 2006. Joining pipe with the hybrid laser-GMAW process: Weld test results and cost analysis. *Welding Journal* 85(6): 66–71.